The current issue and full text archive of this journal is available at
www.emeraldinsight.com/0961-5539.htm

Vibrational effect on heat transfer and entropy generation in an elliptic porous cavity

Shohel Mahmud and Roydon Andrew Fraser
Department of Mechanical Engineering, University of Waterloo, Waterloo, Canada

Received 26 May 2004
Revised 23 February 2005
Accepted 13 April 2005

Abstract

Purpose – Free convection inside a square, circular, or elliptic cavity with gravity oscillation is a special class of problems. In a microgravity environment, the reduction or elimination of natural convection can enhance the properties and performances of materials such as crystals. However, aboard orbiting spacecrafts, all objects undergo low-amplitude broadband perturbed accelerations, or g-jitter, caused by crew's activities, orbiter maneuvers, equipment vibrations, solar drag, and other sources. Therefore, there is a growing interest in understanding the effects of these perturbations on the systems' behavior. There is no information of flow, heat transfer, and irreversibility analyses in the current literature that considers such a situation in a porous medium. This motivates this paper to conduct the current research.

Design/methodology/approach – As a special case, an elliptic enclosure is considered here. The enclosure is filled with a porous medium whose flow is modeled by the Darcy momentum equation. The full governing differential equations are simplified by the Boussinesq approximation and solved by a finite volume method. Prandtl number (*Pr*) is fixed at 1.

Findings – The average Nusselt number (*Nu*), Bejan number (*Be*), and entropy generation number (*Ns*) are adopted to characterize the heat transfer and irreversibilities. Gravity oscillation introduces periodic behavior to the *Nu*, *Be*, and *Ns* rate. Depending on the frequency and the Rayleigh number (*Ra*), three distinguishable regimes of ψ behavior are identified: periodic and synchronous, periodic and asynchronous, and non-periodic and asynchronous.

Research limitations/implications – Current research is valid only for laminar Darcy type flow situation in the porous media.

Originality/value – This paper will extend the existing theory of thermovibrational convection to porous media.

Keywords Convection, Porous materials, Vibration

Paper type Research paper

Nomenclature

A = area of the cavity (m^2)
a = half of the major axis of the cavity (m)
b = half of the minor axis of the cavity (m)
Be = Bejan number (equation (19)).
C_p = specific heat of the fluid ($J\,kg^{-1}\,°C^{-1}$)
C_s = specific heat of the solid matrix ($J\,kg^{-1}\,°C^{-1}$)
Ec_m = modified Eckert number $(= u_0^2 D^2/(C_p K \Delta T))$
K = permeability of the porous media (m^2)
KE = kinetic energy (J)
Ns = entropy generation number (equation (18))
Nu = Nusselt number (equations (20) and (22))
Pr = Prandtl number, $(= \nu/\alpha)$.
Ra = Rayleigh number (equation (3)).
S'''_{gen} = entropy generation rate ($W\,m^{-3}\,K^{-1}$)
S'''_0 = characteristics entropy transfer rate (equation (16))
T = temperature of the fluid (°C)
T_0 = reference temperature (°C)

International Journal of Numerical Methods for Heat & Fluid Flow
Vol. 16 No. 2, 2006
pp. 151-171

0961-5539
DOI 10.1108/09615530610644244

t = time (s)
u^* = = x-component of the velocity ($m\,s^{-1}$)
v^* = = y-component of the velocity ($m\,s^{-1}$)
u = = x-component of the dimensionless velocity ($= u^*/u_0$)
v = = y-component of the dimensionless velocity ($= v^*/u_0$)
u_0 = reference velocity, ($= \alpha/D$).
x^* = horizontal distance (m)
y^* = vertical distance (m)
x = dimensionless horizontal distance ($= x^*/D$)
y = dimensionless vertical distance ($= y^*/D$)
$\forall$ = volume of the cavity (m^3)

Greek symbols
α = thermal diffusivity of the fluid ($m^2\,s^{-1}$)
β = thermal expansion coefficient of the fluid ($°C^{-1}$)
ψ^* = streamfunction ($m^2\,sec^{-1}$)
ψ = dimensionless streamfunction ($= \psi^*/\alpha$)
Θ = dimensionless temperature, ($= (T - T_0)/\Delta T$)
ω^* = angular frequency (Hz)
ω = dimensionless angular frequency (equation (3)).
ρ = density of the fluid ($kg\,m^{-3}$)
ρ_s = density of the solid matrix ($kg\,m^{-3}$)
τ = dimensionless time ($= t\,\alpha/(D^2\,\sigma)$)
σ = empirical constant (equation (3))
ν = kinematic viscosity of the fluid ($m^2\,sec^{-1}$)
ϕ = porosity of the porous media
θ = angle of orientation of the cavity

Introduction

The study of free convection heat transfer inside enclosures (porous or non-porous) is a persistent problem in a variety of situations. During the last two decades, many articles have been published in this field. For a comprehensive reference, see Bejan (1984). Free convection inside a square, circular, or elliptic cavity with gravity oscillation is a special class of problems. In a low gravity or microgravity environment, the reduction or elimination of natural convection can enhance the properties and performances of materials such as crystals (Hirita *et al.*, 2001). However, aboard orbiting spacecrafts, all objects undergoes low-amplitude broadband perturbed accelerations, or g-jitter, caused by crew's activities, orbiter maneuvers, equipment vibrations, solar drag, and other sources. Therefore, there is a growing interest in understanding the effects of these perturbations on the systems' behavior. The reference articles by Hirata *et al.* (2001), Biringen and Danabasoglu (1990), Gershuni and Zhukhovitskiy (1986), Goldhirsch *et al.* (1989), Kamotani *et al.* (1981), Kondos and Subramanian (1996), Ferguson and Lilleleht (1996), Gershuni *et al.* (1983), Sharifulin (1986) and Wadih and Roux (1988) give a good sense of the scope of the flow field and thermal field behavior inside or around rectangular enclosures and cylindrical geometries under gravity oscillation. Until 2003, there has been no reported research activities that systematically elucidates the effects of gravity oscillation on the natural convection heat transfer and entropy generation rates inside elliptic enclosures in a microgravity environment. Furthermore, there has been no research of the entropy generation nature inside a square or circular cavity under gravity oscillation. Most of the published articles, related to elliptic geometry, report the external flow around cylinders or the internal flow inside annuli. The reference articles by Chmaissem *et al.* (2002), Moukalled and Acharya (1996), Chen and Wang (1996), Hossain *et al.* (1998), Mota *et al.* (2000), Badr and Shamsher (1993), Schreiber and Singh (1987) and Cheng and Chao (1996) indicate the scope of heat transfer and flow problems of elliptic cylinders in different flow situations, boundary conditions, and geometric configurations.

Most of the published analyses have been restricted, from a thermodynamic point of view, to only First Law (of thermodynamics) analyses. The contemporary trend in the field of heat transfer and thermal design is to perform a Second Law (of thermodynamics) analysis, and a design-related analysis of entropy generation minimization (Bejan, 1996). The latter is employed to model and optimize real devices that owe their thermodynamic imperfection to heat transfer, mass transfer, and fluid flow irreversibilities. Entropy generation minimization is also known as "thermodynamic optimization" in engineering, where it was first developed, and more recently as "finite space-time thermodynamics" in physics (Bejan, 2002). Such a method combines the most basic concepts of heat transfer, fluid mechanics, and thermodynamics into simple models. They are used in the optimization of real (irreversible) devices and processes, subject to finite-size and finite-time constraints that are, in fact, responsible for the irreversible operation of the device. Therefore, for the proper use of this method, an analyst must know the behavior of the system's irreversibilities in terms of the entropy generation and the variation of the irreversibilities with the system parameters, including the flow parameters, transport properties, and geometry.

Therefore, the entropy generation characteristics are examined, along with the nature of the heat transfer inside a porous elliptic cavity, by numerically solving the fully nonlinear time-dependent momentum and energy equations in a two-dimensional (2D) Cartesian frame. More specifically, the cavity is divided into two symmetrical parts by the *y*-axis in Figure 1, and the wall of each part of the cavity is perfectly isothermal, but differentially heated. The gravity oscillation is assumed to follow a perfect sine wave. The results in this work are presented for a range of Rayleigh numbers (*Ra*) ($10 \leq Ra \leq 5,000$), the angles of orientation ($-90° \leq \theta \leq +90°$), and different frequencies of oscillation.

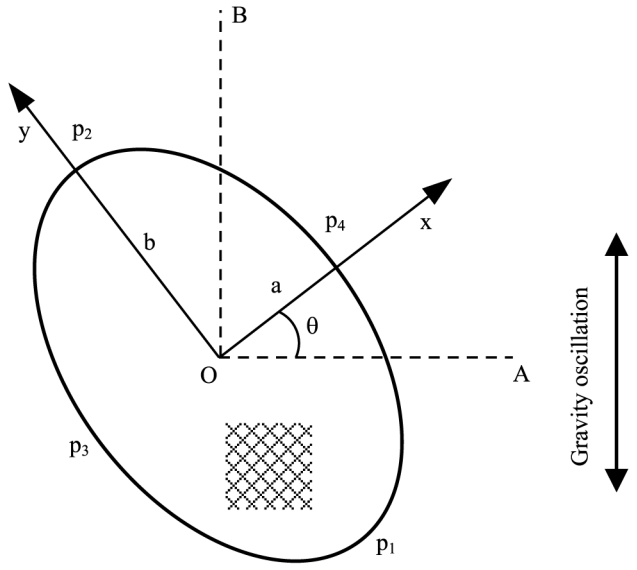

Figure 1.
Schematic diagram of the problem under consideration

Equations and numerical methods

Figure 1 shows the domain to be analyzed and the adopted coordinate system a and b represent the corresponding half of the minor axis and the major axis, respectively. All asterisked quantities in this paper represent the dimensional forms of the considered variables. Fluid, in a 2D cavity with an elliptic cross-section, is subjected to a sinusoidal acceleration that is parallel to the vertical line OB (Figure 1) in a zero-gravity field. The cavity wall of the left symmetrical part (about the y-axis) is cold, and the wall of right part is hot. It is assumed that the cavity is completely filled with fluid. The uneven density of the fluid, originating from the temperature difference of the walls, yields a buoyancy force inside the cavity. This buoyancy force, together with the fluctuating acceleration, drives the convective motion. It is also assumed that the saturated porous medium is isotropic in its thermal conductivity and follows the Darcy model (Bejan, 1984). Finally, the set of non-dimensional governing equations, in terms of the stream function ψ and temperature Θ, are:

$$\frac{\partial^2\psi}{\partial x^2}+\frac{\partial^2\psi}{\partial y^2}=Ra\frac{\partial\Theta}{\partial x}\sin(\omega\tau) \tag{1}$$

and

$$\frac{\partial\Theta}{\partial\tau}+\frac{\partial\psi}{\partial y}\frac{\partial\Theta}{\partial x}-\frac{\partial\psi}{\partial x}\frac{\partial\Theta}{\partial y}=\frac{\partial^2\Theta}{\partial x^2}+\frac{\partial^2\Theta}{\partial y^2}, \tag{2}$$

where

$$x=\frac{x^*}{2b}, y=\frac{y^*}{2b}, \psi=\frac{\psi^*}{\alpha}, \Theta=\frac{T-T_0}{\Delta T}, \Delta T=T_{\text{hot}}-T_{\text{cold}}, T_0=\frac{T_{\text{hot}}+T_{\text{cold}}}{2}$$

$$\tau=t\left(\frac{\alpha}{(2b)^2\sigma}\right), Ra=\frac{gK\beta\Delta T2b}{\alpha\nu}, \omega=\frac{\omega^*\sigma(2b)^2}{\alpha}, u=\frac{\partial\psi}{\partial y}, v=-\frac{\partial\psi}{\partial x} \tag{3}$$

$$\sigma=\frac{\phi\rho C_{\text{p}}+(1-\phi)\rho_{\text{s}}C_{\text{s}}}{\rho C_{\text{p}}},$$

subject to the following boundary conditions:

$$\begin{aligned}&\text{For } \tau>0\\ &\psi=0 \text{ and } \Theta=0.5 \text{ along } p_1-p_4-p_2\\ &\psi=0 \text{ and } \Theta=-0.5 \text{ along } p_1-p_3-p_2.\end{aligned} \tag{4}$$

The meanings of the different parameters in equations (1)-(4) are given in the nomenclature section.

To solve the governing equations, we develop a computer code (NATURE, written in FORTRAN 77). NATURE is a finite volume code, but is based on a finite element approach to represent the geometry. The finite volume method proceeds by integrating

equations (1) and (2) over a fixed control volume, which, by using Gauss's Theorem, results in:

$$\int_s \frac{\partial \psi}{\partial x}\,\mathrm{d}n_x + \int_s \frac{\partial \psi}{\partial y}\,\mathrm{d}n_y = \int_\upsilon Ra\,\frac{\partial \Theta}{\partial x}\sin(\omega\tau)\,\mathrm{d}\upsilon \tag{5}$$

and

$$\int_\upsilon \frac{\partial \Theta}{\partial \tau}\,\mathrm{d}\upsilon + \int_s u\Theta\,\mathrm{d}n_x + \int_s v\Theta\,\mathrm{d}n_y = \int_s \frac{\partial \Theta}{\partial x}\,\mathrm{d}n_x + \int_s \frac{\partial \Theta}{\partial y}\,\mathrm{d}n_y \tag{6}$$

where υ and s denote the volume and surface integrals, respectively, and $\mathrm{d}n_x$ and $\mathrm{d}n_y$ are the differential Cartesian components of the outward normal surface vector. The surface integrals are integrations of the fluxes of the conserved quantities, whereas the volume integrals represent the source terms. What defines the control volume is an important distinguishing feature of the finite volume implementations. After, the computational domain is discretized into elements, the control volume surfaces are defined by element mid-planes. This approach has been used by other researchers such as Schneider and Raw (1986, 1987). The procedure creates a control volume for each node so that with the boundary of each interior control volume is defined by eight line-segments in 2D. This arrangement is shown in Figure 2(a). The integral equations, equations (5) and (6), are applied to each discrete control volume, created by this technique. The continuous volume integrations are relatively easy to convert to a discrete form, as will demonstrate later. Since the continuous surface integrations are more involved, they are converted to a discrete form by evaluating them at the integration points (ip). The location of the integration points for one flux element is shown in Figure 2(b) for a 2D quadrilateral element. The surface fluxes must be discretely represented at the integration points to complete the conversion of the continuous equations to their discrete counterparts. The discrete forms of the integral equations are written as:

$$\sum_{\mathrm{ip}}\left(\frac{\partial \psi}{\partial x}\Delta n_x\right)_{\mathrm{ip}} + \sum_{\mathrm{ip}}\left(\frac{\partial \psi}{\partial y}\Delta n_y\right)_{\mathrm{ip}} - Ra\frac{\partial \Theta}{\partial x}\sin(\omega\tau)\mathrm{Vol} = 0 \tag{7}$$

and

$$\mathrm{Vol}\left(\frac{\Theta - \Theta^0}{\Delta\tau}\right) + \sum_{\mathrm{ip}}(u\,\Delta n_x)^0_{\mathrm{ip}}\Theta_{\mathrm{ip}} + \sum_{\mathrm{ip}}(v\,\Delta n_y)^0_{\mathrm{ip}}\Theta_{\mathrm{ip}} - \sum_{\mathrm{ip}}\left(\frac{\partial \Theta}{\partial x}\Delta n_x\right)_{\mathrm{ip}} - \sum_{\mathrm{ip}}\left(\frac{\partial \Theta}{\partial y}\Delta n_y\right)_{\mathrm{ip}} = 0 \tag{8}$$

where Vol is the volume of the control volume, the ip denotes an integration point, Σ is the summation over all the integration points of the surface, Δn_x and Δn_y are the discrete outward surface vectors, Δt is the time step, 0 refers to mean "at the old time level", and the overbar on the source terms indicates an average value for the control volume.

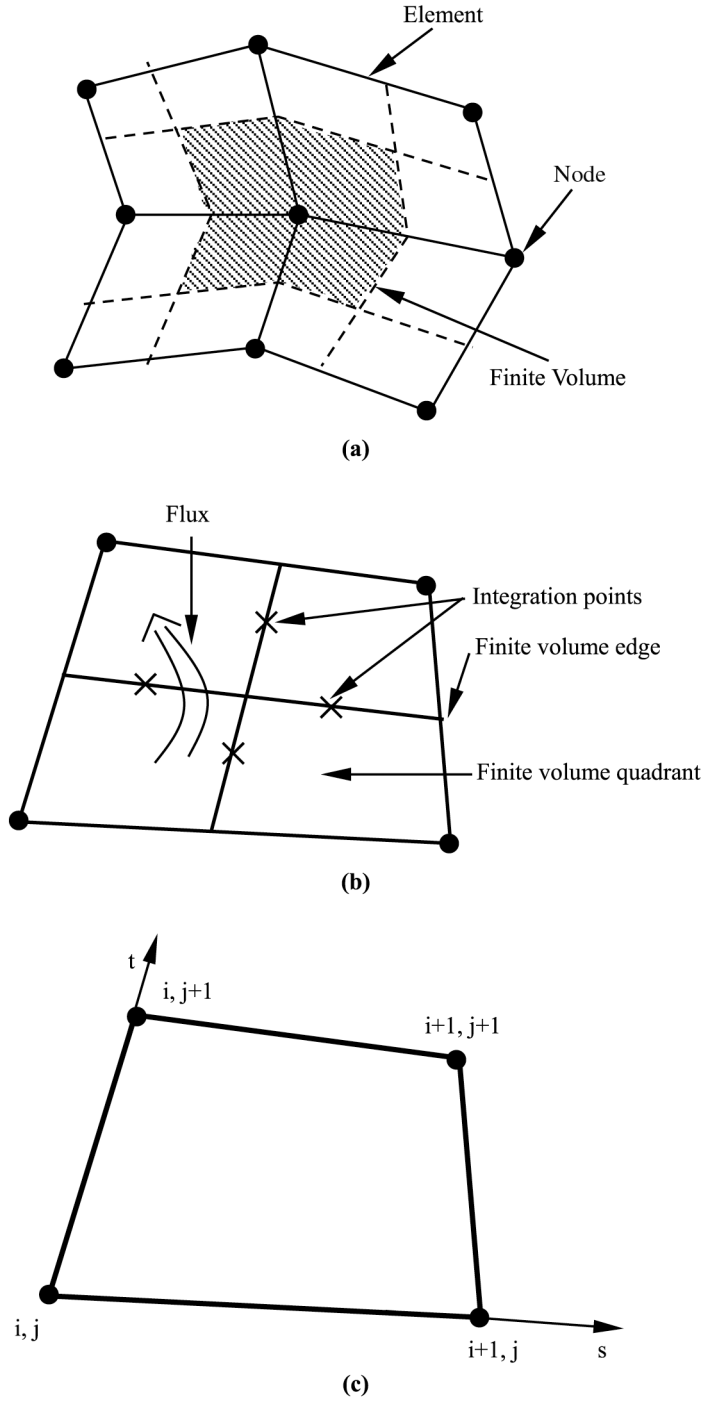

Figure 2.
(a) The definition of the control volume, (b) integration point definition for a 2D quadrilateral element, and (c) four noded flux element

The time step term:

$$\mathrm{Vol}\left(\frac{\Theta - \Theta^0}{\Delta\tau}\right), \tag{9}$$

is a first-order accurate backwards Euler approximation of the transient term. Also, called the "lumped mass" approximation. Since it is robust and fully implicit, it creates no time step limitation and is easy to implement.

Following the standard finite element approach, shape functions are used to evaluate the derivatives for all the diffusion terms. For instance, for a derivative in the x direction at ip:

$$\left.\frac{\partial\Phi}{\partial x}\right|_{\mathrm{ip}} = \sum_n \left.\frac{\partial N_n}{\partial x}\right|_{\mathrm{ip}} \Phi_n, \tag{10}$$

where the summation is over all the shape functions for the element. In equation (10), Φ represents any variable, for example, Θ and ψ. The Cartesian derivatives of the shape functions can be expressed in terms of their local derivatives via the Jacobian transformation matrix:

$$\begin{pmatrix} \frac{\partial N}{\partial x} \\ \frac{\partial N}{\partial y} \end{pmatrix} = \begin{pmatrix} \frac{\partial x}{\partial s} & \frac{\partial y}{\partial s} \\ \frac{\partial x}{\partial t} & \frac{\partial y}{\partial t} \end{pmatrix}^{-1} \begin{pmatrix} \frac{\partial N}{\partial s} \\ \frac{\partial N}{\partial t} \end{pmatrix}. \tag{11}$$

For the (i, j) flux element (Figure 2(c)), the domain of the element can be defined in terms of the local, non-orthogonal coordinates s and t by:

$$\begin{aligned} x(s,t) &= N_1 x_{i,j} + N_2 x_{i+1,j} + N_3 x_{i,j+1} + N_4 x_{i+1,j+1} \\ y(s,t) &= N_1 y_{i,j} + N_2 y_{i+1,j} + N_3 y_{i,j+1} + N_4 y_{i+1,j+1}, \end{aligned} \tag{12}$$

where the shape functions N are given by:

$$N_1 = \frac{1}{4}(1-s)(1-t),\ \ N_2 = \frac{1}{4}(1+s)(1-t),\ \ N_3 = \frac{1}{4}(1-s)(1+t),\ \ N_4 = \frac{1}{4}(1+s)(1+t). \tag{13}$$

To discretize the advection terms, a modified central differencing scheme, based on the upwind differencing scheme (UDS) plus the correction, is used which is mathematically expressed as:

$$\Phi_{\mathrm{ip}} = \Phi_{\mathrm{up}} + (\Delta\Phi_{\mathrm{ip}})^0, \ \text{ with } \ \Delta\Phi_{\mathrm{ip}} \approx \frac{\Delta x}{2}\left(\frac{\partial\Phi}{\partial x}\right)_{\mathrm{ip}}. \tag{14}$$

Equation (14) shows the approximation of Φ_{ip} for the x-direction only. The approximation of the source term is shown in Das *et al.* (2003) and is not repeated here. After all the cell face fluxes and sources are summed, the discretized transport equation reduces to the following algebraic equation:

$$A_P \Phi_P + \sum_{\text{nb}} A_{\text{nb}} \Phi_{\text{nb}} = Q_\Phi, \tag{15}$$

where the coefficient A_{nb} contains the convective and diffusive flux contribution, and Q_Φ represents the source term. The system of equations is solved by using the TDMA solver (Ferziger and Peric, 1996). The entire computational domain is subdivided by unequally spaced control volumes (= 14,848). The time increment ($\Delta\tau$) is 10^{-4} in most of the cases, but sometimes, especially at a high *Ra*, smaller values are chosen to confirm the accuracy of the results.

Entropy generation

The dimensionless form of the entropy generation rate (S'''_{gen}) is the entropy generation number (*Ns*) (Bejan, 1996) which is the ratio of entropy generation rate (S'''_{gen}) to the characteristic entropy transfer rate (S'''_0). For the present problem, S'''_0 can be estimated from the following:

$$S'''_0 = \frac{k(\Delta T)^2}{D^2 T_0^2}. \tag{16}$$

For the porous medium which follows the Darcy model, the local rate of the entropy generation (S'''_{gen}) can be calculated (Bejan, 1984) from the following:

$$S'''_{\text{gen}} = \frac{k}{T_0^2}(\vec{\nabla} T)^2 + \frac{\mu}{K T_0}(\vec{\mathbf{V}})^2. \tag{17}$$

By using equations (16) and (17), one can express *Ns* as:

$$Ns = \frac{S'''_{\text{gen}}}{S'''_0} = \left[\left(\frac{\partial \Theta}{\partial x}\right)^2 + \left(\frac{\partial \Theta}{\partial y}\right)^2\right] + \frac{Ec_{\text{m}} \times Pr}{\Omega}\left[\left(\frac{\partial \psi}{\partial x}\right)^2 + \left(\frac{\partial \psi}{\partial y}\right)^2\right]. \tag{18}$$

Equation (18) consists of two parts. The first part (the first bracketed term at the right-hand side of equation (18)) is the irreversibility due to the finite temperature gradient and is generally referred to the heat transfer irreversibility (HTI). The second part (the second bracketed term in equation (18)) is the contribution of the fluid friction irreversibility (FFI) to the entropy generation. Therefore, the overall entropy generation for a particular problem is an internal competition between the HTI and the FFI. Usually, natural convection problems at low and moderate *Ra* are dominated by the HTI. The *Ns* is reliable for generating entropy generation profiles or maps, but fails to give any idea whether the fluid friction or the heat transfer dominates. Two alternate parameters, the irreversibility distribution ratio (Φ) and the Bejan number (*Be*), are becoming increasingly popular among the Second Law analysts. The *Be*, which is the ratio of HTI to the *Ns*, is mathematically expressed as:

$$Be = \frac{\text{HTI}}{\text{HTI} + \text{FFI}}. \tag{19}$$

The *Be* ranges from 0 to 1. Accordingly, $Be = 1$ is the limit at which the HTI dominates, $Be = 0$ is the opposite limit at which the irreversibility is dominated by the

fluid friction effects, and $Be = 1/2$ is the case in which the heat transfer and fluid friction entropy generation rates are equal.

Results and discussions

For the benchmarking purpose, a square porous cavity is selected. The remaining results in this paper are calculated for an elliptic cavity with an aspect ratio of $2(= b/a)$.

Benchmarking

For benchmarking, a differentially heated square porous cavity under a constant gravity force is considered. The gravity force is parallel to the isothermal walls, and the two remaining walls are adiabatic. The test case is similar to the cases in the references (Baytas and Pop, 1999; Walker and Homsy, 1978; Gross *et al.*, 1986; Manole and Lage, 1992; Moya *et al.*, 1987). The average *Nu* is calculated for three different *Ra* ($Ra = 10$, 100 and 1,000), and compared to those in the literature (Baytas and Pop, 1999; Walker and Homsy, 1978; Gross *et al.*, 1986; Manole and Lage, 1992; Moya *et al.*, 1987). These comparisons, summarized in Table I, confirm that the results are in good agreement with the previous results. Therefore, we are confident that the proposed numerical method and the results are accurate.

Steady-state limit

The flow and thermal fields behavior in the steady-state limit (i.e. the results with no gravity fluctuation) are presented first. In this limit, the $\sin(\omega\tau)$ term in equation (1) is temporarily dropped. The Isothermal lines inside the cavity are shown in Figure 3 for the seven different *Ra*. A total of 21 isothermal lines are plotted in each figure with an interval of $\Delta\Theta = 0.05$. The corresponding streamfunction plots are shown in Figure 4. The fluid, adjacent to the right wall, is heated and begins to flow upwards, turns at the top, and mixes with the downward stream of the cold fluid, adjacent to the left wall. This causes the circulation inside the cavity which is very weak at $Ra = 10$. The strength of the circulation is reported by the value of the maximum streamfunction (ψ_{max}) in the figure title. Also, it is evident that the thermal field is almost unaffected by the flow field at such a low *Ra*. A conduction-like isotherms are observed at $Ra = 10$ which is symmetric about the vertical centerline of the cavity. The streamlines resemble concentric ellipsis. With an increase in the *Ra*, for example, $Ra = 50$, the symmetric pattern of the isothermal lines starts to break that is observed at a low *Ra*. A convection current develops inside the cavity at this *Ra*, affecting the thermal field. The core of the streamline tilts slightly towards the left wall, but the streamlines near

	Nu_{av}		
	$Ra = 10$	$Ra = 100$	$Ra = 1{,}000$
Baytas and Pop (1999)	1.079	3.16	14.06
Walker and Homsy (1978)	–	3.10	12.96
Gross *et al.* (1986)	–	3.14	13.45
Manole and Lage (1992)	–	3.12	13.64
Moya *et al.* (1987)	1.065	2.80	–
Present prediction	1.079	3.14	13.82

Table I.
Comparison of average *Nu* with some previous numerical results

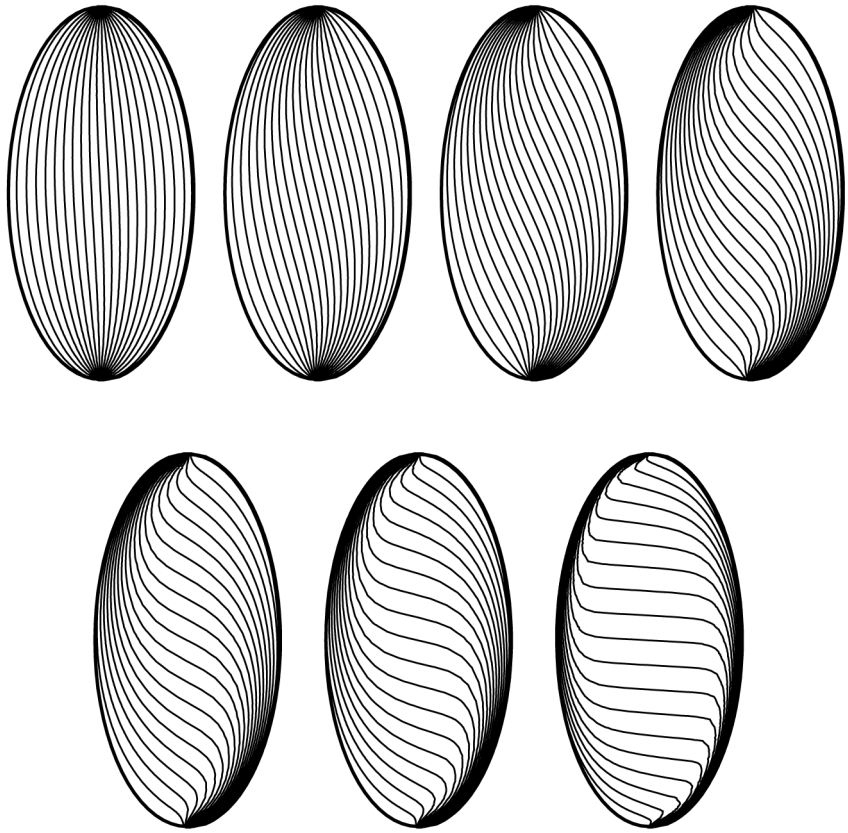

Figure 3.
Isothermal lines at (a) $Ra = 10$, (b) $Ra = 50$, (c) $Ra = 100$, (d) $Ra = 250$, (e) $Ra = 500$, (f) $Ra = 1{,}000$ and (g) $Ra = 5{,}000$

the cavity wall have the same elliptic shape as before. The isothermal lines are even more asymmetric at $Ra = 100$. Two small portions at the bottom of the right wall and the top of the left wall indicate a higher concentration of the isothermal lines, as seen in Figure 3. These portions are a clear indication of the thermal spots where the temperature gradient as well as the heat transfer rate is higher than the central portion of the cavity. A convective distortion of the isothermal lines is observed at $Ra = 250$ and 500. The thermal spots extend as the Ra increases, and the streamlines are no longer elliptic in shape. When a further increase in the Ra elongates the thermal spots along the wall, a boundary layer type of flow is observed at $Ra = 1,000$ and $Ra = 5,000$. The magnitude of the fluid velocity at a high Ra is relatively small in the middle portion of the cavity, compared to the magnitude of the fluid velocity near the cavity walls. The steady-state average Nusselt number ($Nu_{\text{av, steady}}$) and entropy generation number ($Ns_{\text{av, steady}}$) are calculated by the following equations:

$$Nu_{\text{av,steady}} = \frac{2}{\pi(a+b)} \int_S \left. \frac{\partial \Theta}{\partial n} \right|_{\text{wall}} \mathrm{d}s, \tag{20}$$

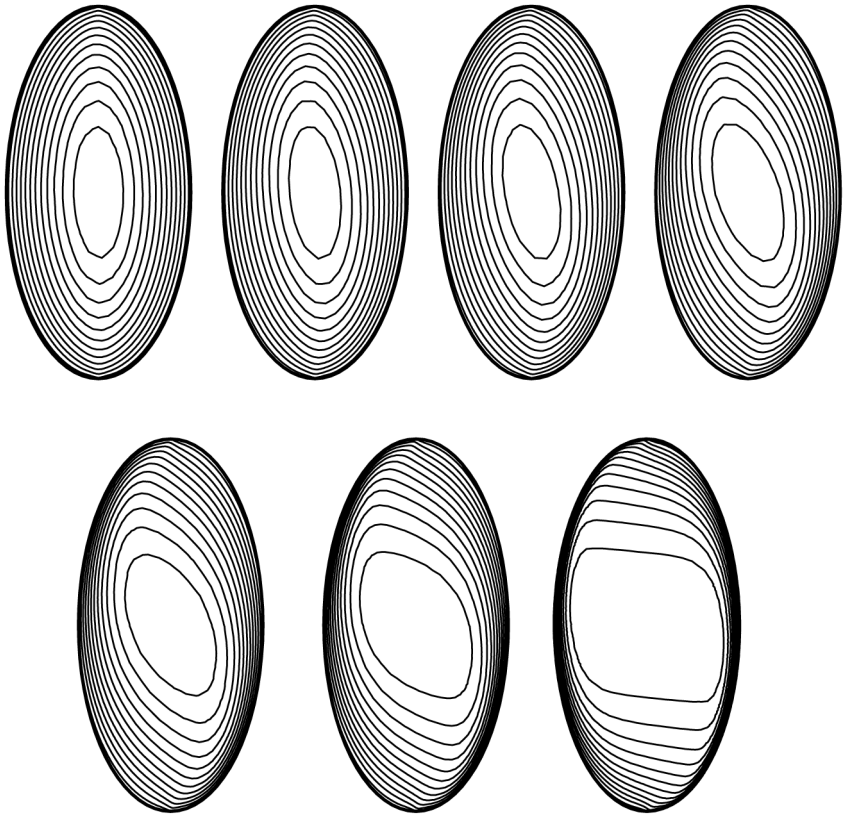

Figure 4.
Streamlines at (a) $Ra = 10$ ($\psi_{max} = 0.5456$), (b) $Ra = 50$ ($\psi_{max} = 2.6353$), (c) $Ra = 100$ ($\psi_{max} = 4.8937$), (d) $Ra = 250$ ($\psi_{max} = 9.8594$), (e) $Ra = 500$ ($\psi_{max} = 15.3667$), (f) $Ra = 1{,}000$ ($\psi_{max} = 22.7433$), and (g) $Ra = 5{,}000$ ($\psi_{max} = 52.0875$)

$$Ns_{\text{av,steady}} = \frac{1}{\forall}\int_{\forall} Ns \, d\forall, \tag{21}$$

where s is the distance along the hot wall, S is the arc length of $p_1 - p_4 - p_2$, and $\forall$ represents the volume of the cavity. Figure 5 shows the distribution of the $Nu_{\text{av, steady}}$, as a function of the Ra, at five different θ. Two distinct zones, depending on the $Nu_{\text{av, steady}}$ and Ra relationship, are shown in Figure 5. At the conduction regime (the low Ra), the average Nu is the same in magnitude for all θ and independent of the Ra's variation. At the convection dominated regime, the relationship between the $Nu_{\text{av, steady}}$ and Ra is linear (in a log-log plot) in nature. At this regime, the magnitude of the $Nu_{\text{av, steady}}$ depends on the θ at a particular value of Ra. Figure 6 shows the variation of the $Nu_{\text{av, steady}}$ with θ at three different Ra. The angular location, $\theta = -90°$, is the most unstable position for the fluid (a hot bottom wall and cold top wall), and $\theta = +90°$ is the most stable position (a cold bottom wall and hot top wall). The heat transfer rate exhibits its maximum at $\theta \approx -10°$ approximately for all the Ra. Any change in the θ, either in a clockwise or an anti-clockwise direction from this position, causes a decrease in the $Nu_{\text{av, steady}}$. The $Ns_{\text{av, steady}}$ increases as Ra is increased for all θ (Figure 7). The variation of the $Ns_{\text{av, steady}}$ with the θ (Figure 8) indicates a similar trend to that seen in the $Nu_{\text{av, steady}} - \theta$ profiles.

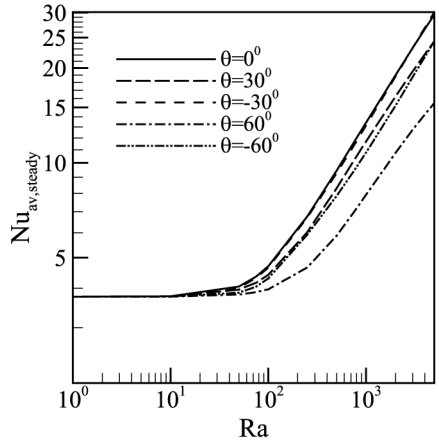

Figure 5.
Steady state average *Nu* as a function of *Ra* at different angles of orientation

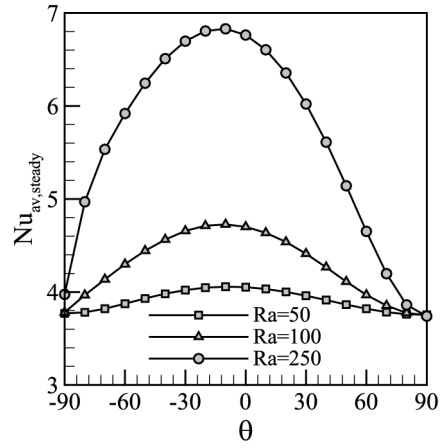

Figure 6.
Steady state average *Nu* as a function of angle of orientation at different *Ra*

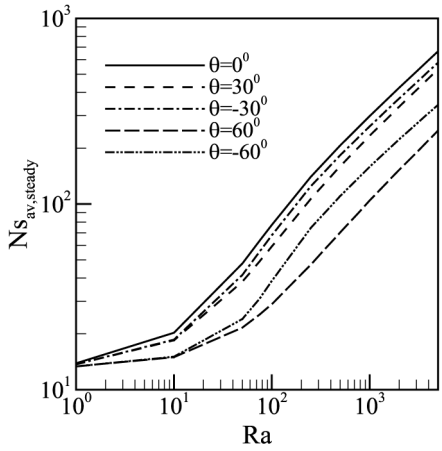

Figure 7.
Steady state average *Ns* as a function of *Ra* at different angles of orientation

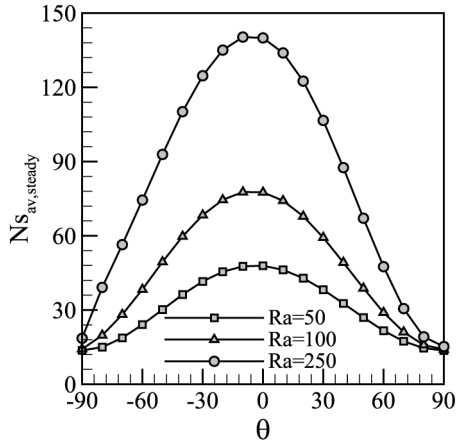

Figure 8.
Steady state average *Ns* as a function of angle of orientation at different *Ra*

Vibrational convection

We start with the heat transfer characteristics inside the cavity. The rate of the heat transfer is measured in terms of a dimensionless *Nu*. Once the gravity vibration is introduced (at time $\tau = \tau_0$), it takes some time to attain the convective motion inside the cavity (the determination of this time is beyond the scope of this paper). For the details about the setup time and instability, refer to Gershuni and Lyubimov (1997). At a particular time, $\tau = \tau_0 + m\Delta\tau, m = 0, 1, 2\ldots,$ the normal component of the temperature gradient (i.e. $\partial\Theta/\partial n|_w$) near the wall is measured which is a function of the time and distance. An integration is then carried out as follows:

$$Nu_{av} = Nu_{av}(\tau) = \frac{1}{\pi(a+b)} \oint_{\Gamma} \left|\frac{\partial\Theta}{\partial n}\right| ds, \tag{22}$$

along the whole boundary of the cavity (Gershuni and Lyubimov, 1997) to attain the spatially averaged *Nu* (Nu_{av}) as a function of the dimensionless time. For the limited time interval, $0 > \tau \geq 4$, the variation of the Nu_{av} is reported as a function of time (τ) in Figure 9 for four different *Ra*. In a real simulation, the time interval is much longer than this time interval. It is evident from Figure 9 that an induced gravity oscillation introduces true periodic behavior of the average heat transfer rate. Since we used the absolute value of the normal component of the temperature gradient (equation (22)) during the calculation of the Nu_{av}, the fluctuation of Nu_{av} appears in the positive half of the $Nu_{av} - \tau$ plot. The periodic response of Nu_{av} is synchronized with the forced acceleration; i.e. the same period of oscillation as that of the forced acceleration. This synchronous relation is shown in Figures 9 and 10. The phase portraits are generated by plotting the value of the Nu_{av} (Figure 10) and the Ns_{av} (Figure 11) with a 1/4 period phase lag (denoted by δ) against the unlagged value of the Nu_{av} and Ns_{av}. For both cases (Figures 9 and 10), the closed loop in the phase portrait indicates the synchronous relation between the gravity oscillation and system parameters (Nu_{av}, Ns_{av}, etc.). At the upper extreme of the oscillation, $\omega\tau = (2m-1)\pi/2, m = 1, 2, 3\ldots,$ the magnitude of

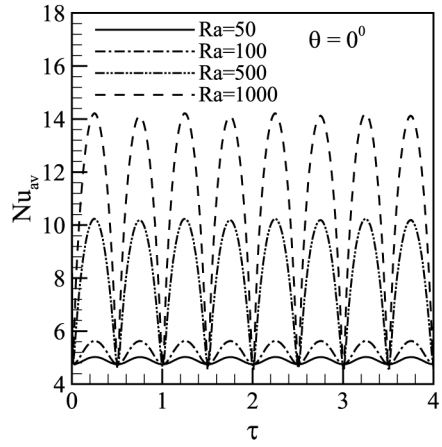

Figure 9.
Average Nu (Nu_{av}) as a function of dimensionless time (τ) at $\omega = 2\pi$ and $Ra = 50$, 100, 500, and 1,000

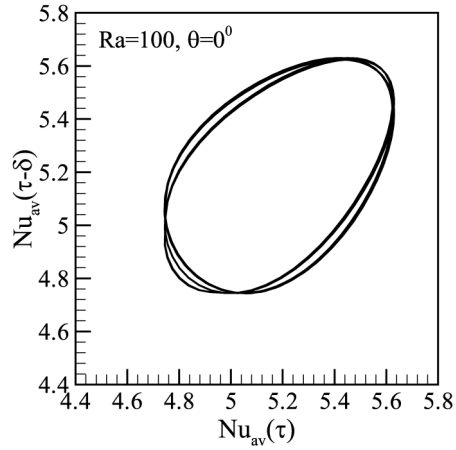

Figure 10.
Phase portrait of Nu at $Ra = 100$ and $\theta = 0°$

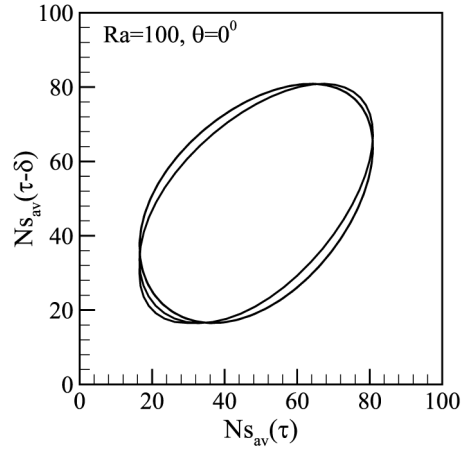

Figure 11.
Phase portrait of Ns at $Ra = 100$ and $\theta = 0°$

the Nu_{av} approaches the corresponding value of the $Nu_{av,\ steady}$. At the lower extreme of the oscillation, $\omega\tau = m\pi$, $m = 1, 2, 3\ldots$, the gravity force disappears. The heat transfer inside the cavity occurs in the conduction mode.

The *Ns* and *Be* are calculated by equations (18) and (19), respectively, as functions of the spatial coordinates and time. The volume averaged value of the *Ns* (Ns_{av}) and *Be* (Be_{av}) can be calculated by the following:

$$Ns_{av} = Ns_{av}(\tau) = \frac{1}{\forall}\int_{\forall} Ns(x, y, \tau)\, d\forall \tag{23}$$

and

$$Be_{av} = Be_{av}(\tau) = \frac{1}{\forall}\int_{\forall} Be(x, y, \tau)\, d\forall \tag{24}$$

where $\forall$ represents the volume of the cavity. The Ns_{av} is plotted as a function of the dimensionless time in Figure 12 for three different values of the *Ra*. We know that the $Ns_{av} - \tau$ behavior is similar to the $Nu_{av} - \tau$ behavior. The periodic response of the Nu_{av} synchronizes with the gravity oscillation. At a particular time, the irreversibility is higher at a high *Ra*. The maximum value of the Ns_{av} is obtained for any *Ra* when gravity oscillation reaches its upper extreme ($\omega\tau = (2m - 1)\pi/2$, $m = 1, 2, 3\ldots$). In the absence of gravity ($\omega\tau = m\pi$, $m = 1, 2, 3\ldots$), Ns_{av} of each *Ra* is the same.

The Be_{av} distribution remains synchronized with the gravity oscillation. Figure 13 shows the distribution of the Be_{av} as a function of dimensionless time at $Ra = 50$, 100, 500, and 1,000, respectively. The time gap is set between 1 and 3 for convenience. At the lower extreme of the gravity oscillation, due to the absence of gravity force, there is no convective motion inside the cavity. This causes the maximum dominance of the HTI, when the Be_{av} reaches its maximum value (= 1). This is true for all the *Ra*. For all the *Ra*, the Be_{av} shows its minimum at the upper extreme of the oscillation, where the convection motion is well set and the FFI has a reasonable domination over the HTI.

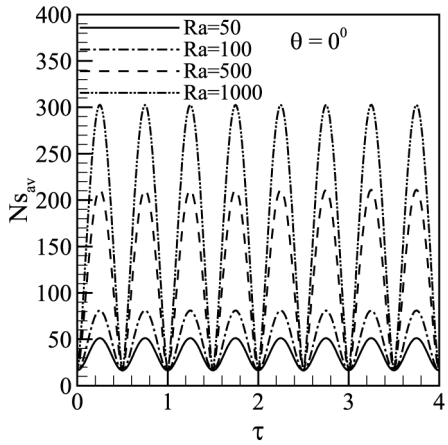

Figure 12.
Average *Ns* (Ns_{av}) as a function of dimensionless time (τ) at $\omega = 2\pi$ and $Ra = 50$, 100, 500, and 1,000

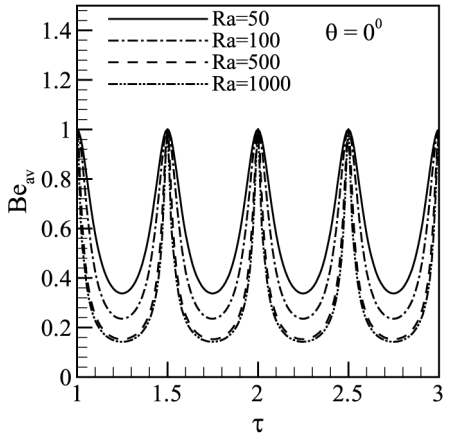

Figure 13.
Average Be (Be_{av}) as a function of dimensionless time (τ) at $\omega = 2\pi$ and $Ra = 50$, 100, 500, and 1,000

This minimum value of the Be_{av} is lower in magnitude for a higher Ra. At a higher Ra (for example, $Ra = 1,000$) a boundary layer type flow is commonly observed in a steady-state and constant gravity situation. However, for the situation where the flow field is affected by the gravity oscillation, there is no immediate formation of the hydrodynamic and thermal boundary layers. At the beginning of the oscillation (for example, at $\tau = 2$ in Figure 13), no gravity force and no FFI exists. The conduction dominated heat transfer contributes a little to the HTI. With the absence of FFI, the HTI equals the Ns_{av} and the corresponding Be_{av} equals 1 (Figure 13). A nonzero gravity component appears just after the beginning time ($\tau = 2$), which immediately sets the convective motion inside the cavity so that a positive contribution to the overall entropy generation rate is now derived from the FFI. Then, the Be_{av} rapidly drops to a small value within a small period of time, since a hydrodynamic boundary layer forms, and the thermal boundary layer is still in its developing stage. After formation, the additional modification of the hydrodynamic boundary layer, with time, is slow, and by this time, the thermal boundary layer is finally shaped with the increasing temperature gradient, as well as the HTI. Slowly, the Be_{av} drops to its minimum value up to the upper extreme of the oscillation.

Figures 14-16 portray the temporal variations of the Nu_{av}, Ns_{av}, and Be_{av} at different θ, respectively. Since the time dependent nature of these parameters at $\theta = 0°$ has been presented (Figures 9, 12, and 13), it is omitted here. Any inclination of the cavity, either clockwise or anti-clockwise, presents a different picture of the variations of the parameters which exhibit a certain pattern of periodic repetition with time. For example, the variation of the Nu_{av} at $\theta = +60°$ is taken for the time interval $\tau = 1$-2 (Figure 14). During the first half of this time interval, $\tau = 1$-1.5, the Nu_{av} increases with τ from its minimum value (at $\tau = 1$), peaks at $\tau = 1.25$, and then decreases with the increasing τ, repeating its minimum value again at $\tau = 1.5$. During the second half of the interval, $\tau = 1.5$-2, a similar distribution pattern is observed, but now the magnitude of the Nu_{av} is higher than the magnitude at the first half except at $\tau = 2$, where the minimum value of the Nu_{av} is repeated. In contrast, for $\theta = -60°$, the same

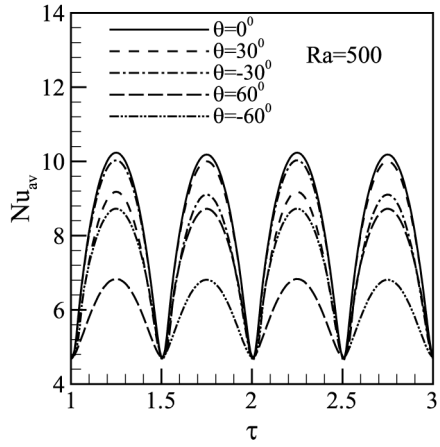

Figure 14.
Average Nu (Nu_{av}) as a function of dimensionless time (τ) at $\omega = 2\pi$ and different angles of orientation

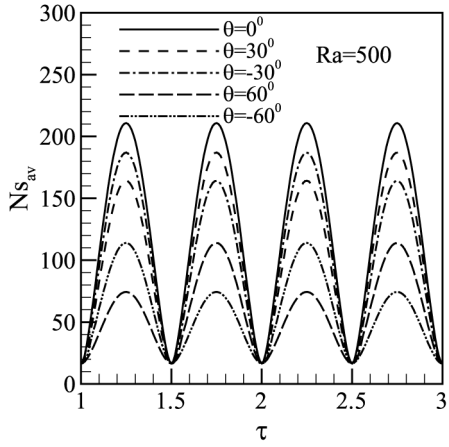

Figure 15.
Average Ns (Nu_{av}) as a function of dimensionless time (τ) at $\omega = 2\pi$ and different angles of orientation

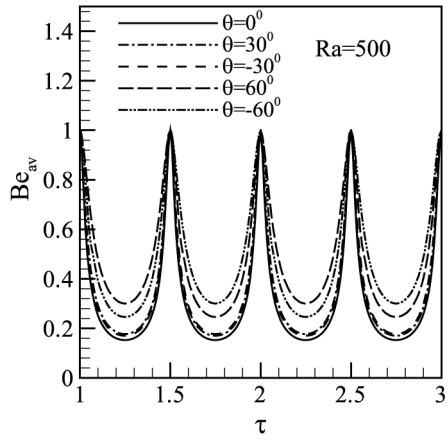

Figure 16.
Average Be (Nu_{av}) as a function of dimensionless time (τ) at $\omega = 2\pi$ and different angles of orientation

pattern of distribution is observed for the Ns_{av} (Figure 15), but the opposite distribution pattern is seen for the Be_{av} (Figure 16).

The spatially averaged kinetic energy KE_{av} (Hirata *et al.*, 2001) is calculated according to the following equation:

$$KE_{av} = KE_{av}(\tau) = \frac{1}{2A}\int\int (u^2 + v^2)\,dx\,dy, \tag{25}$$

where A is the cross-sectional area of the cavity. The KE_{av} serves as a global indicator of responses (Hirata *et al.*, 2001). The distribution of the KE_{av}, as a function of τ, is shown in Figure 17 for two Ra ($Ra = 50$ and 100). The synchronous behavior of the $KE_{av} - \tau$ profile with gravity oscillation is similar to the $Nu_{av} - \tau$ or $Ns_{av} - \tau$ profile, as described earlier.

To this point, only a single frequency ($\omega = 2\pi$) has been considered. The remainder of this paper is devoted to identifying the effect of frequency on the ranges of the Ra in which the flow and heat transfer variations are periodic and synchronous, periodic and asynchronous, or non-periodic and asynchronous (Figure 18(a)-(d)). The streamfunctions (ψ) in Figure 18(a)-(c) are monitored at the center ($x = y = 0$) of the cavity. The patterns of the variation in ψ, Nu_{av}, and Ns_{av}, with time, are more or less the same at a particular combination of ω and Ra. The PSR natures of the results are broadly summarized in Figure 18(d), as a function of ω and Ra. Each of the 132 computational runs used to construct Figure 18(d) are obtained after the initial computational transients decay. Figure 18(a) shows a typical example of a periodic and synchronous response (PSR) with forced acceleration. The periodic response provides a solution with the same period as the forced acceleration. A synchronous response describes a result with the same sine wave shape as the forced acceleration. The square symbols in Figure 18(d) represent the PSR cases; the open square symbol identifies the case in Figure 18(a). Figure 18(b) is a typical example of a periodic but asynchronous response (PAR). The circle symbols in Figure 18(d) represent the PAR cases; the open circle symbol signifies the case in Figure 18(b). The sharp spikes in ψ, seen in Figure 18(b), are used as a the characteristic feature of the asynchronous response.

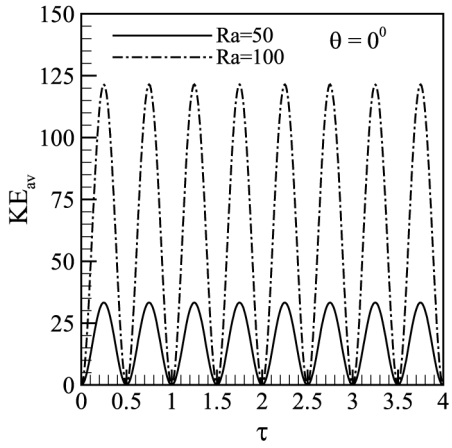

Figure 17.
Average kinetic energy (KE_{av}) as a function of dimensionless time (τ) at $\omega = 2\pi$ and $Ra = 50$, 100

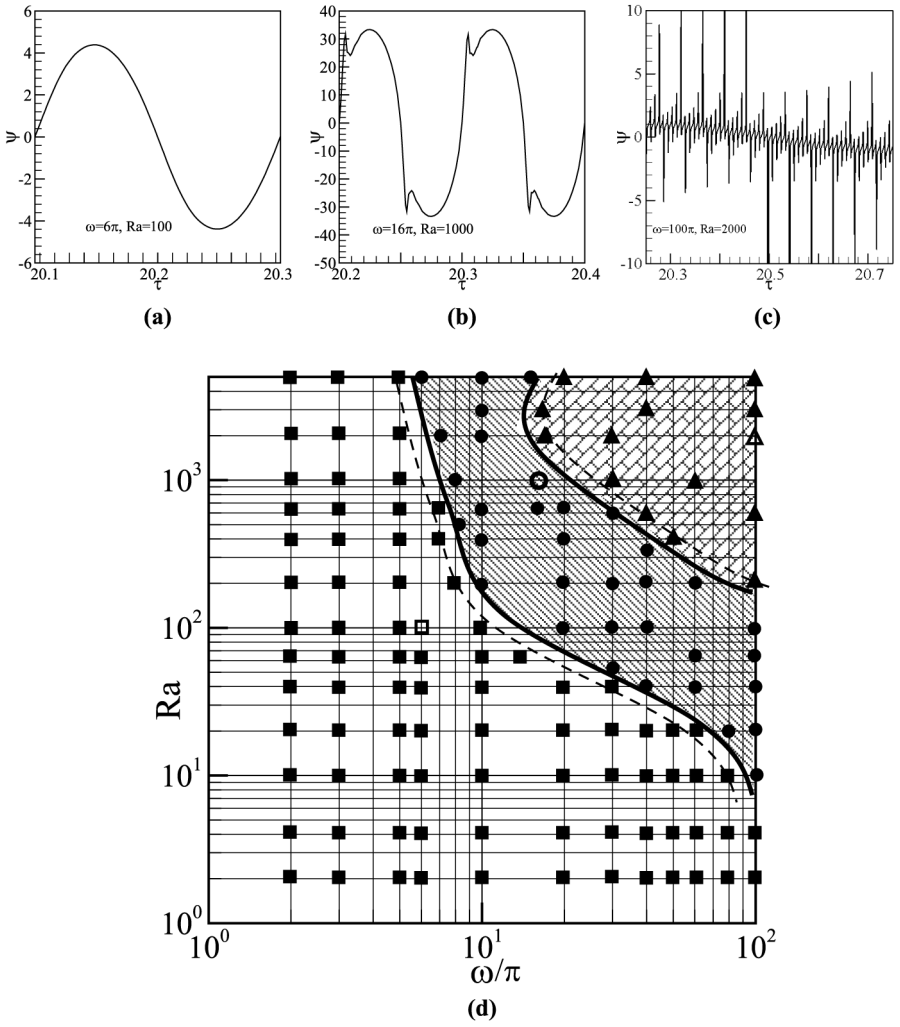

Figure 18.
Time evolution of streamfunction ψ at $(x, y) = (0, 0)$ when (a) $\omega = 6\pi$, $Ra = 100$, (b) $\omega = 16\pi$, $Ra = 1{,}000$, (c) $\omega = 100\pi$, $Ra = 2{,}000$ and (d) summary of the periodicity

The heavy solid line in Figure 18(d) separates the synchronous and asynchronous responses; however, more simulations are required in the region, bounded by the dashed line and solid line, to better identify the critical periodic-synchronous-to-periodic-asynchronous transition *Ra*. Figure 18(c) is a typical non-periodic and asynchronous response (NAR). The triangular symbols in Figure 18(d) represent the NAR cases; the open triangle symbol denotes the case in Figure 18(c). A second heavy solid line is used in Figure 18(d) to separate the periodic-synchronous and non-periodic-asynchronous responses; however, more simulations are needed in the region, bounded by the solid line and dashed line, to better identify the critical periodic-asynchronous-to-non-periodic-asynchronous transition *Ra*.

Conclusions

A numerical solution to the governing momentum and energy equations for a porous elliptic cavity is presented. Heat transfer, HTI, and total irreversibility under gravity oscillation condition are examined. The average *Nu*, *Be*, and *Ns* are adopted to characterize the heat transfer and irreversibilities. In the steady-state limit, both the *Nu* and *Ns* exhibit little variation of the *Ra*, when the *Ra* is considerably smaller in magnitude ($Ra > 100$). For a higher *Ra*, both the *Nu* and *Ns* indicate a linear variation of *Ra* on a log-log plot. For all the values of the *Nu* and *Ns* investigated, the maximum is at or near a $-10°$ angle of orientation. Gravity oscillation introduces periodic behavior to the *Nu*, *Be*, and *Ns* rate. Depending on the frequency and the *Ra*, three distinguishable regimes of ψ behavior are identified:

- periodic and synchronous (PSR);
- periodic and asynchronous; and
- non-periodic and asynchronous.

References

Badr, H.M. and Shamsher, K. (1993), "Free convection from an elliptic cylinder with major axis vertical", *Int. J. Heat Mass Transfer*, Vol. 36, pp. 3593-602.

Baytas, A.C. and Pop, I. (1999), "Free convection in oblique enclosures filled with a porous medium", *Int. J. Heat Mass Transfer*, Vol. 42, pp. 1047-57.

Bejan, A. (1984), *Convection Heat Transfer*, Wiley, New York, NY.

Bejan, A. (1996), *Entropy Generation Minimization*, CRC Press, New York, NY.

Bejan, A. (2002), "Fundamental of exergy analysis, entropy generation minimization, and the generation of flow architecture", *Int. J. Energy Research*, Vol. 26, pp. 545-65.

Biringen, S. and Danabasoglu, G. (1990), "Computation of convective flow with gravity modulation in rectangular cavities", *J. Thermophys*, Vol. 4, pp. 357-65.

Chen, Y.M. and Wang, K.C. (1996), "Numerical and experimental studies on natural convection from a horizontal elliptic cylinder", *J. Chinese Inst. Chem. Eng.*, Vol. 27, pp. 353-62.

Cheng, C.H. and Chao, C.C. (1996), "Numerical prediction of the buoyancy-driven flow in the annulus between horizontal eccentric elliptical cylinders", *Numer. Heat Transfer (Part A)*, Vol. 30, pp. 283-303.

Chmaissem, W., Suh, S.J. and Daguenet, M. (2002), "Numerical study of the Boussinesq model of natural convection in an annular space: having a horizontal axis bounded by circular and elliptical isothermal cylinders", *Appl. Thermal Eng.*, Vol. 22, pp. 1013-25.

Das, P.K., Mahmud, S., Tasnim, S.H. and Islam, A.K.M.S. (2003), "Effect of surface waviness and aspect ratio on heat transfer inside a wavy enclosure", *Int. J. Num. Meth. for Heat & Fluid Flow*, Vol. 13, pp. 1097-122.

Ferguson, F.T. and Lilleleht, L.U. (1996), "Thermovibrational convection in a vertical cylinder", *Int. J. Heat Mass Transfer*, Vol. 39, pp. 2895-906.

Ferziger, J. and Peric, M. (1996), *Computational Methods for Fluid Dynamics*, Springer, Berlin.

Gershuni, G.Z. and Lyubimov, D.V. (1997), *Thermal Vibrational Convection*, Wiley, New York, NY.

Gershuni, G.Z. and Zhukhovitskiy, Y.M. (1986), "Vibration-induced thermal convection in weightlessness", *Fluid Mech.-Sov. Res.*, Vol. 15, pp. 63-84.

Gershuni, G.Z., Zhukhovitsky, E.M. and Sharifulin, A.N. (1983), "Vibrational thermal convection in cylindrical cavity", *Numer. Meth. Cont. Med. Mech.*, Vol. 14, pp. 21-33.

Goldhirsch, I., Pelz, R.B. and Orszag, S.A. (1989), "Numerical simulation of thermal convection in a two-dimensional finite box", *J. Fluid Mech.*, Vol. 199, pp. 1-28.

Gross, R.J., Bear, M.R. and Hickox, C.E. (1986), "The application of flux-corrected transport (FCT) to high *Ra* natural convection in porous medium", *Proceedings of the 8th International Heat Transfer Conference*, *San Francisco, CA*.

Hirata, K., Sasaki, T. and Tanigawa, H. (2001), "Vibrational effects on convection in a square cavity at zero gravity", *J. Fluid Mech.*, Vol. 445, pp. 327-44.

Hossain, M.A., Alim, M.A. and Rees, D.A.S. (1998), "Effect of thermal radiation on natural convection over cylinders of elliptic cross section", *Acta Mechanica*, Vol. 129, pp. 177-86.

Kamotani, Y., Prasad, A. and Ostrach, S. (1981), "Thermal convection in an enclosure due to vibrations aboard spacecraft", *AIAA J.*, Vol. 19, pp. 511-16.

Kondos, P.A. and Subramanian, R.S. (1996), "Buoyant flow in a two-dimensional cavity due to a sinusoidal gravitational field", *Microgravity Sci. Technol.*, Vol. 9, pp. 143-51.

Manole, D.M. and Lage, J.L. (1992), "Numerical benchmark results for natural convection in a porous medium cavity", *Heat and Mass Transfer in Porous Media, Proceedings of ASME Conference*, HTD-Vol. 216, pp. 55-60.

Mota, J.P.B., Esteves, I.A.A.C., Portugal, C.A.M., Esperanca, J.M.S.S. and Saatdjian, E. (2000), "Natural convection heat transfer in horizontal eccentric elliptic annuli containing saturated porous media", *Int. J. Heat Mass Transfer*, Vol. 43, pp. 4367-79.

Moukalled, F. and Acharya, S. (1996), "Natural convection in the annulus between concentric horizontal circular and square cylinders", *J. Thermophys. Heat Transfer*, Vol. 10, pp. 524-31.

Moya, S.L., Ramos, E. and Sen, M. (1987), "Numerical study of natural convection in a tilted rectangular porous material", *Int. J. Heat Mass Transfer*, Vol. 30, pp. 741-56.

Schneider, G.E. and Raw, M.J. (1986), "A skewed, positive influence coefficient upwinding procedure for control-volume-based finite element convection-diffusion computations", *Numer. Heat Transfer*, Vol. 8, pp. 1-26.

Schneider, G.E. and Raw, M.J. (1987), "Control-volume finite element method for heat transfer and fluid flow using collocated variables – 1. Computational procedure", *Numer. Heat Transfer*, Vol. 11, pp. 363-90.

Schreiber, W.C. and Singh, S.N. (1987), "Natural convection in a stratified fluid between confocal horizontal elliptical cylinders", *Numer. Heat Transfer*, Vol. 11, pp. 183-97.

Sharifulin, A.N. (1986), "Supercritical vibration-induced thermal convection in a cylindrical cavity", *Fluid Mech.-Sov. Res.*, Vol. 15, pp. 28-35.

Wadih, M. and Roux, B. (1988), "Natural convection in a long vertical cylinder under gravity modulation", *J. Fluid Mech.*, Vol. 193, pp. 391-415.

Walker, K.L. and Homsy, G.M. (1978), "Convection in a porous cavity", *J. Fluid Mech.*, Vol. 87, pp. 449-74.

Corresponding author
Shohel Mahmud is the corresponding author and can be contacted at: smahmud@uwaterloo.ca